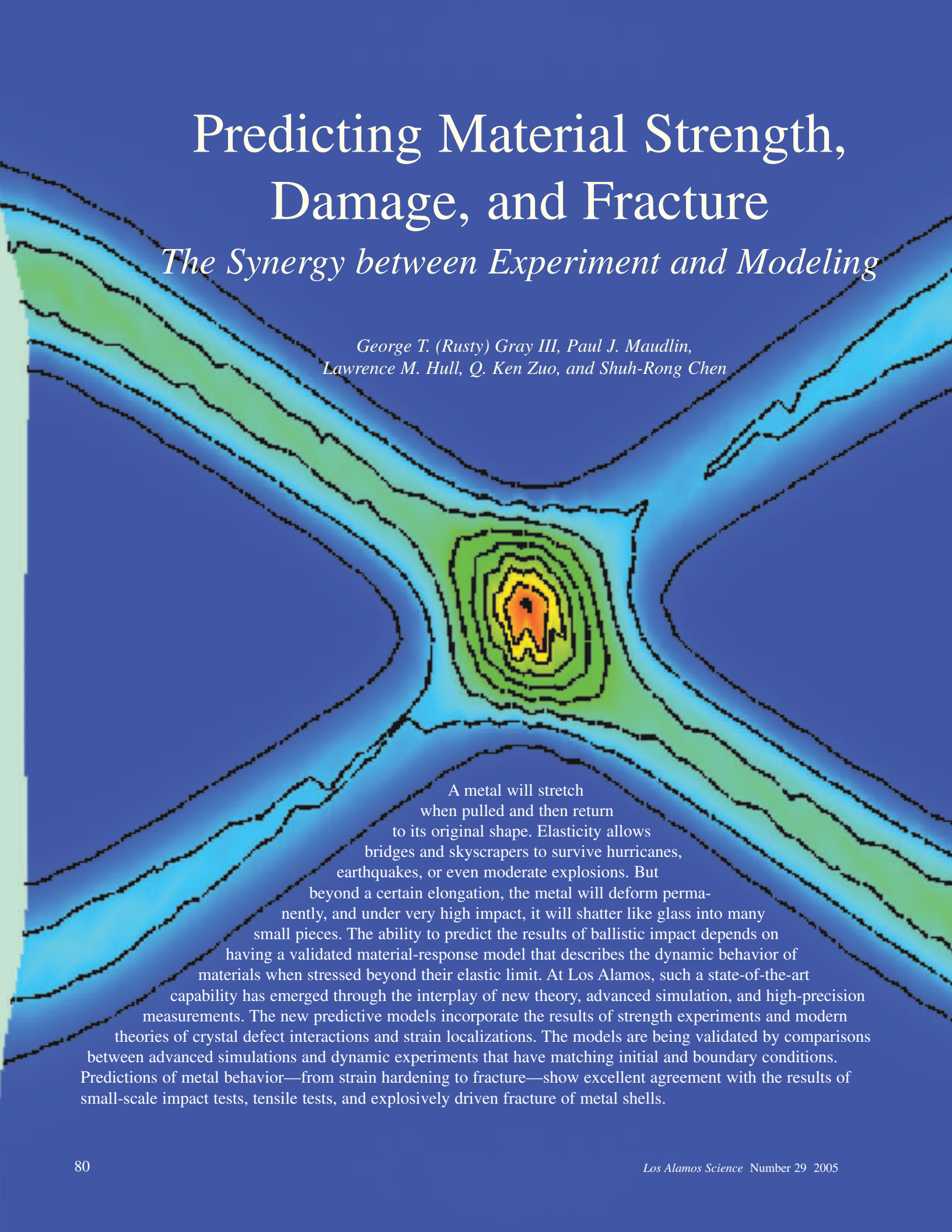



# Predicting Material Strength, Damage, and Fracture

## *The Synergy between Experiment and Modeling*

*George T. (Rusty) Gray III, Paul J. Maudlin,  
Lawrence M. Hull, Q. Ken Zuo, and Shuh-Rong Chen*



A metal will stretch when pulled and then return to its original shape. Elasticity allows bridges and skyscrapers to survive hurricanes, earthquakes, or even moderate explosions. But beyond a certain elongation, the metal will deform permanently, and under very high impact, it will shatter like glass into many small pieces. The ability to predict the results of ballistic impact depends on having a validated material-response model that describes the dynamic behavior of materials when stressed beyond their elastic limit. At Los Alamos, such a state-of-the-art capability has emerged through the interplay of new theory, advanced simulation, and high-precision measurements. The new predictive models incorporate the results of strength experiments and modern theories of crystal defect interactions and strain localizations. The models are being validated by comparisons between advanced simulations and dynamic experiments that have matching initial and boundary conditions. Predictions of metal behavior—from strain hardening to fracture—show excellent agreement with the results of small-scale impact tests, tensile tests, and explosively driven fracture of metal shells.



**F**rom the first time one sharp object was used to shape another or cause another to fracture, the mechanical properties of materials—strength, ductility, and susceptibility to fracture—have shaped human history. Materials influence human life so profoundly that some have become synonymous with different eras—the Stone Age, the Bronze Age, the Iron Age, and the Nuclear Age. It is very possible that the current era, marked by people's growing dependency on electronics, may soon be dubbed the Silicon Age.

During the past eras, materials were selected almost exclusively on the basis of hands-on experience—one material shows favorable properties over another for a given application. But a new capability is now emerging—that of predicting material behavior and designing and engineering custom materials with predetermined characteristics. This trend could, in principle, lead to the age of “predictive materials technology,” but only time will tell. What we demonstrate in this article is an emerging capability to predict and engineer the behavior of metals—their mechanical response under extreme loading conditions.

Engineering the response of metals and alloys to loading is an age-old trade, extending from the famous fifth century steels of Damascus to the aluminum alloys that enabled the modern era of civilian aviation. Manufacturing recipes were typically developed through trial and error, but during the years leading up to World War I, scientists and engineers conducted the first systematic studies and began to under-

stand how the relationship between the applied stress, or force over area, and the resulting strain, or change in length, varied with temperature, strain rate, and stress state. That knowledge was quickly applied to critical wartime needs: high-speed manufacturing of metal parts (including high-speed wire drawing and cold-rolling of metal parts) and advances in ballistics, armor, and detonation physics. Spinoffs from those early studies led to increasingly sophisticated materials of relevance to defense, transportation, and communications.

In the last four decades, defense-oriented research has pushed the frontier of knowledge beyond standard stress-strain relationships to the complex mechanisms that occur under impact, namely, deformation, damage evolution, and fracture of metals and alloys. The basic mechanisms controlling those processes began to be understood, and the resulting models were used to estimate material response during high-speed impact, or high strain-rate, situations both natural and man-made. Familiar examples include automotive crash-worthiness; aerospace impacts, including foreign-object damage, such as that caused when a jet engine accidentally ingests a bird or a meteorite impacts a satellite; structural accelerations such as those occurring during an earthquake; high-rate manufacturing processes such as high-rate forging and machining; and conventional ordinance behavior and armor/antiarmor interactions. Within the past two decades, as computer power has grown and materials models have become more predictive, the R&D community has used, wherever possible, large-scale

three-dimensional (3-D) computer simulations of these complex dynamic events in place of direct experimentation. The reasons are twofold: Either an experiment would be prohibitively expensive (a full-scale bird-ingestion test on a commercial jet engine conducted for the Federal Aviation Agency, for example, costs millions of dollars to field), or the system is too difficult to evaluate accurately through experiment (for example, the impact of a meteorite on the space station). In turn, the growing reliance on 3-D simulations of complex engineering systems has led to a growing demand for robust predictive material-response models.

We are developing predictive models for mechanical behavior through the interplay between systematic experiments and theory. In this article, we focus most heavily on the role of experiments in developing and validating mechanical response models. First, we present state-of-the-art experiments to measure very accurately the basic stress-strain relationships of metals and alloys under varying temperatures and strain rates. Second, we discuss the ways in which we measure and model specific damage evolution mechanisms that progress from the loss of load-carrying capacity to fracture. Finally, we present specialized experimental methods, measurements, and models describing the dynamic deformation and failure induced by explosive deformation. Although further experimental research and engineering work remain, the efforts described here demonstrate significant progress in quantifying the dynamic mechanical

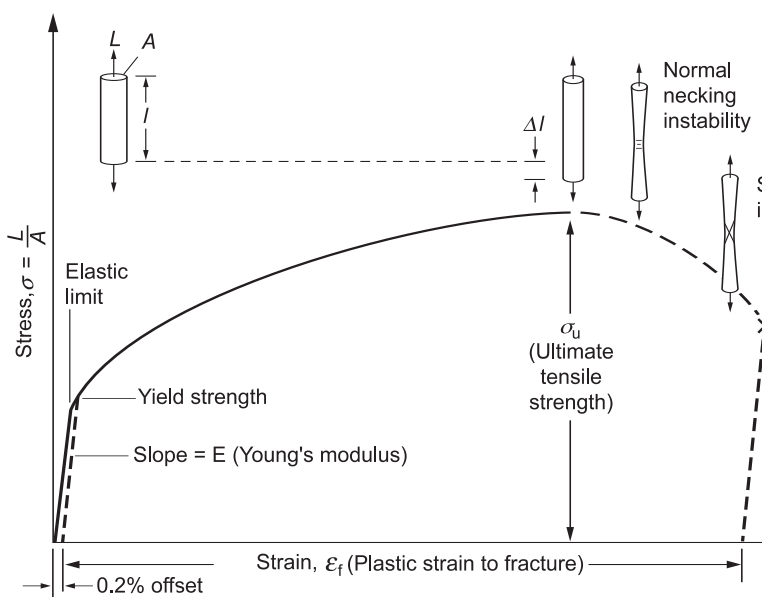


**Figure 1. Tensile Stress-Strain Curve**

The tensile test is the most common test used to measure mechanical properties. Round-bar or sheet samples are gripped at their ends and pulled at constant velocity (nominally, at constant strain rate) until they fail. Load and displacement of the sample are measured and plotted as stress  $\sigma$  (load/cross-sectional area) vs strain  $\epsilon$  (sample elongation/original length). The elastic region, represented by Hooke's law ( $\sigma = E\epsilon$ , where  $E$  is an elastic constant known as Young's modulus), is linear and reversible. The point of deviation from linearity is called the elastic limit and marks the onset of permanent deformation, or plastic strain. Because the onset of deviation is often very gradual, the "yield strength" of a metal is defined as the stress at 0.2% permanent (or plastic) strain. Continued plastic flow beyond the elastic limit produces increasing stress levels, a process called work hardening. During this stage, the sample deforms uniformly, elongating and thinning while the volume remains constant, until work hardening can no longer keep up with the continuing increase in stress caused by the reduction in the sample's cross-sectional area. At this point, the stress goes through a maximum, called the ultimate tensile strength, and the sample begins to deform nonuniformly, or neck, before it fractures in a ductile manner. Necking can reflect either "normal" or shear localization preceding fracture. In soft, annealed fcc metals, the typical total plastic (or permanent) strain immediately before fracture is 20% to 50%.

response of materials and applying those insights to the development of predictive material models of relevance to the defense mission of Los Alamos.

### Mechanical Strength Models: Development and Validation

Standard mechanical strength models for metallic materials spell out the

relationship between stress (load per unit area of material) and the resulting strain (change in length, area, or volume relative to the original dimension) during elastic and stable plastic deformation (see the positive-slope side of the stress-strain curve in Figure 1). However, at some background strain, metals will transition from uniform, or homogeneous, deformation to heterogeneous, or localized, unstable behavior (occur-

ring usually on the negative-slope side of the stress-strain curve). In fact, when an as-received material is pulled at a constant velocity at the boundaries, it follows a stress-strain curve comparable to that in Figure 1. This stress-strain path has four distinct stages: (1) uniform, or homogeneous, deformation and accumulation of background strain, (2) material instability or bifurcation (a condition that indicates loss of load-bearing capacity), (3) transition to heterogeneous, or localized, deformation (in a normal and/or shear mode), and (4) accumulation of damage (small cracks and voids) that ultimately coalesces into a fracture surface. In the description of the experiments and modeling provided in the sections below, both homogeneous and localized deformations are investigated and modeled at macroscopic scales. To be predictive, those models must capture the fundamental relationships connecting the independent variables of stress, strain rate, strain, and temperature to specific bulk material responses such as yield stress or flow stress, strain hardening, texture evolution, evolution of global damage, subsequent heterogeneous damage, such as strain localization and cracking, and finally, material failure.

Moreover, for the applications of interest, we need to predict those responses accurately for such extreme conditions as large deformation and high strain rates, pressures, and temperatures. Our materials models must therefore be based on quantifiable physical mechanisms, characterized with inexpensive direct experiments, and validated through comparisons with results of small-scale and integral tests.

**Standard Measurements of Strength.** One develops a strength model for a particular material by measuring its mechanical properties. The samples of interest are loaded in

compression, tension, or torsion over a range of loading rates and temperatures germane to the application of interest. Various mechanical testing frames are available that achieve nominally constant loading rates for limited plastic strains and, thereby, a constant strain rate. The standard screw-driven or servo-hydraulic testing machines achieve strain rates of up to 5 per second. Specially designed testing machines, typically equipped with high-capacity servo-hydraulic valves and high-speed control and data acquisition instrumentation, can achieve strain rates as high as 200 per second during compression loading. To go even higher, we must employ projectile-driven impacts that induce stress-wave propagation in the sample materials. Chief among these dynamic loading techniques is the split-Hopkinson pressure bar (SHPB) (Gray 2000), which can achieve the highest uniform uniaxial compressive stress loading of a specimen at a nominally constant strain rate of about  $10^3$  per second. In fact, we readily reach strain rates of up to  $2 \times 10^4$  per second and true strains of 0.3 in a single test by using the SHPB. At these stresses and strain rates, however, the uniformity of stress loading and constancy of strain rate are not guaranteed, so care must be exercised.

**Developing a Strength Model for Tantalum.** As shown in Figure 2, we used several of the testing techniques just mentioned to measure the stress-strain response of unalloyed tantalum metal over a wide range of strain rates and temperatures. We then determined the unknown parameters in our strength model by fitting the model to the experimental data. In general, this model predicts flow stress (level of stress needed to produce dislocations in the crystal lattice as a function of strain, strain rate, and temperature), and the mathematical form used is known as the Mechanical Threshold

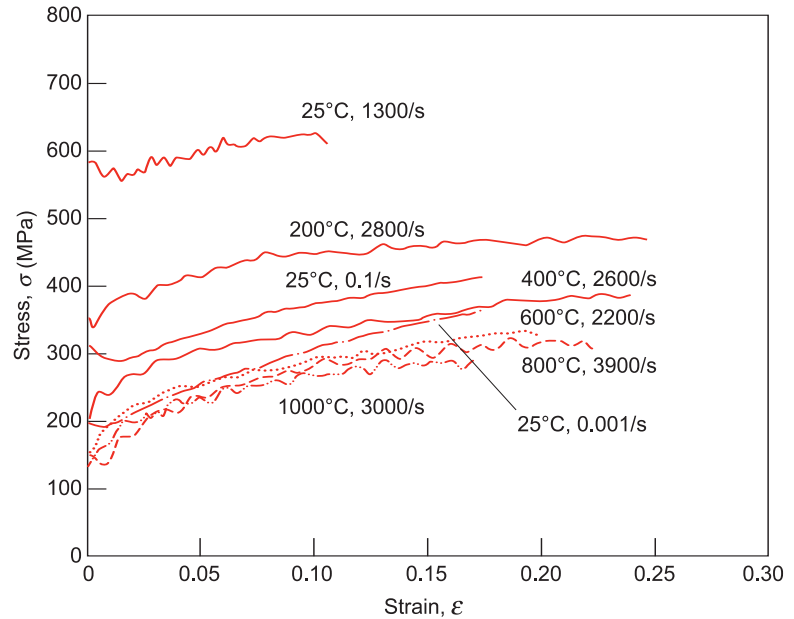


**Figure 2. Compressive Stress-Strain Curves of Unalloyed Tantalum**  
Under lower applied stress, the material deforms more readily as the temperature is increased; conversely, the stress required to deform the material increases as the strain rate (rate of applying stress) is increased.

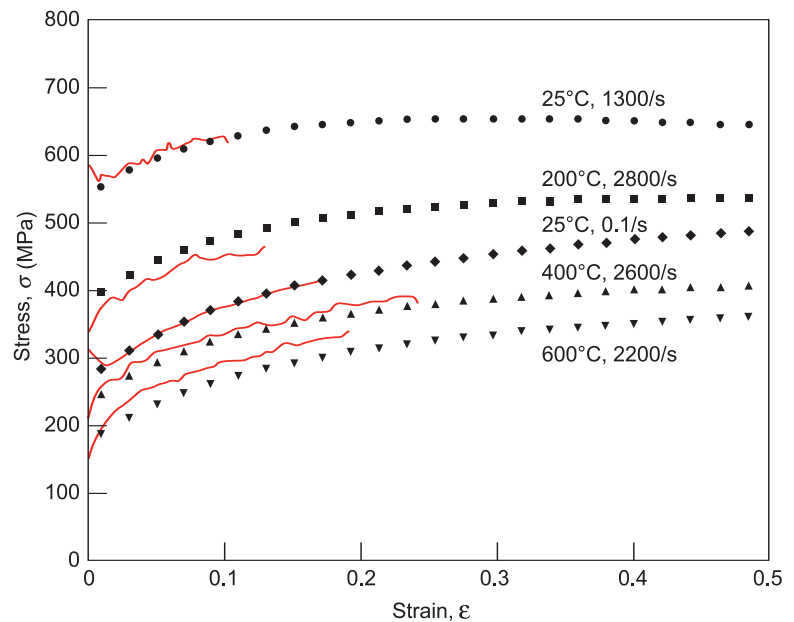


**Figure 3. Mechanical Behavior of Stress-Strain Curves for Unalloyed Tantalum: Experiment vs Calculation**

The experimental mechanical behavior of the stress-strain curves (red lines) of unalloyed tantalum measured for a range of temperatures and loading rates are compared with the fit to the MTS model. Experiment and calculation agree very well.



Strength (MTS) Model (Chen and Gray 1996). Figure 3 gives an example of the characterization of the model parameters for unalloyed tantalum data that show the model accurately capturing the dependence of yielding and strain hardening as strain rate and temperature are varied.

A key feature of the MTS model is an internal state-structure variable that describes the physical property of work hardening that occurs as a metallic specimen deforms plastically. This hardening variable evolves in the context of the model as mobile dislocations (lattice defects), created during the deformation process, interact with other stored-dislocation structures. Those in turn evolve via the dynamic microscale processes of mobile-dislocation storage and stored-dislocation annihilation, both controlled by the independent variables mentioned above. This scalar representation of dislocation behavior by the MTS model is fairly accurate for a large number of metals used in predictive engineering simulation. The model is also easily extended if one uses the concepts of plastic potential and yield surfaces, physically based on micromechanics of polycrystal plasticity, to describe directional (anisotropic) plastic deformation (Maudlin et al. 1999). This extension of the model is illustrated below.

The problem is that many engineering problems, such as foreign-object damage and ballistic impact, involve strain rates of  $10^4$  to  $10^5$  per second, values that are well beyond the range accessible for direct measurement. Is our strength model valid at those higher strain rates? Since we cannot test the model directly, we use it to predict the results of a simple validation test such as the Taylor cylinder impact test. This readily conducted axisymmetric test realizes strain rates as high as  $10^5$  per second and deformations in excess of 100 percent. The MTS model is used

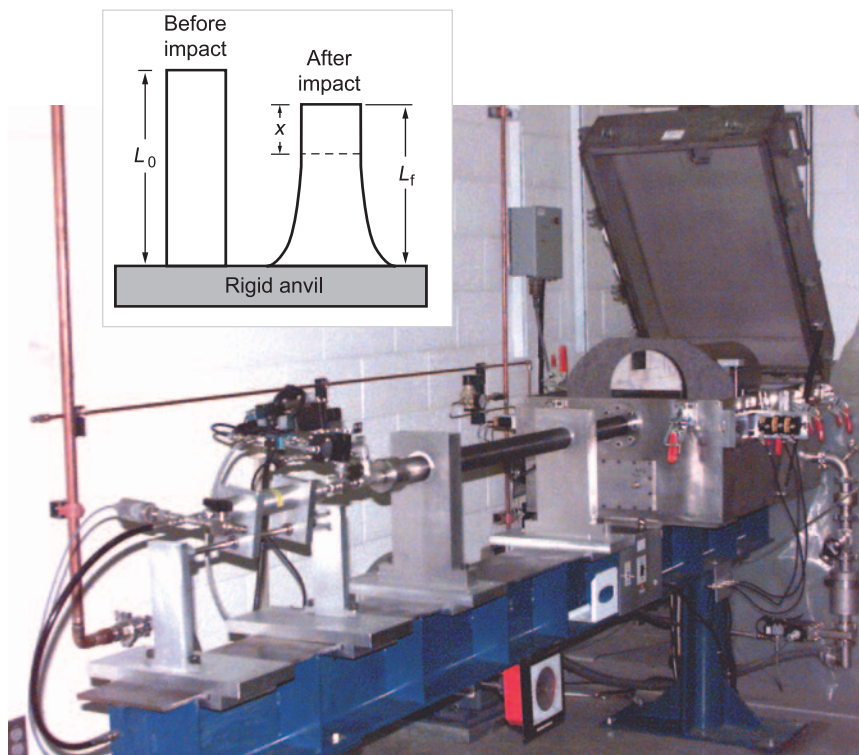


**Figure 4. The Los Alamos Taylor Impact Test Facility**

The photograph shows the apparatus used to fire a small cylindrical test sample at high velocity against a massive, rigid target, and the inset shows the initial and final states of a cylindrical sample.

as part of the constitutive module in a 3-D finite-element continuum mechanics code for simulating the Taylor test, and the results are then compared with post-test geometries (for example, the cylinder side profiles) for several impact velocities.

### The Taylor Impact Test for Validating the Strength Model

The Taylor cylinder impact test shown in Figure 4 was developed during World War II by G. I. Taylor (1948) to screen materials for use in ballistic applications. It entails firing a small solid cylinder rod of some material of interest, typically 7.5 to 12.5 millimeters in diameter by 25 to 40 millimeters in length, at high velocity against a massive and plastically rigid target. As indicated

schematically in the inset to Figure 4, the impact plastically deforms and thereby shortens the Taylor rod by causing material at the impact surface to flow radially outward relative to the rod axis. By assuming simple one-dimensional plastic flow, Taylor related the fractional change in the rod length (difference between the final length  $L_f$  and the initial length  $L_0$ ) to the flow stress, one point on the stress-strain curve in Figure 1.

The Taylor impact test represents an escalation of complexity relative to tests made with the split-Hopkinson pressure bar. Rather than measuring the stress-strain response at a uniform stress state and strain rate, a Taylor test involves gradients of stress, strain, and strain rate integrated over time to produce a final strain distribution. In fact, the Taylor test is most often used to intentionally probe the deformation responses of metals and alloys in the

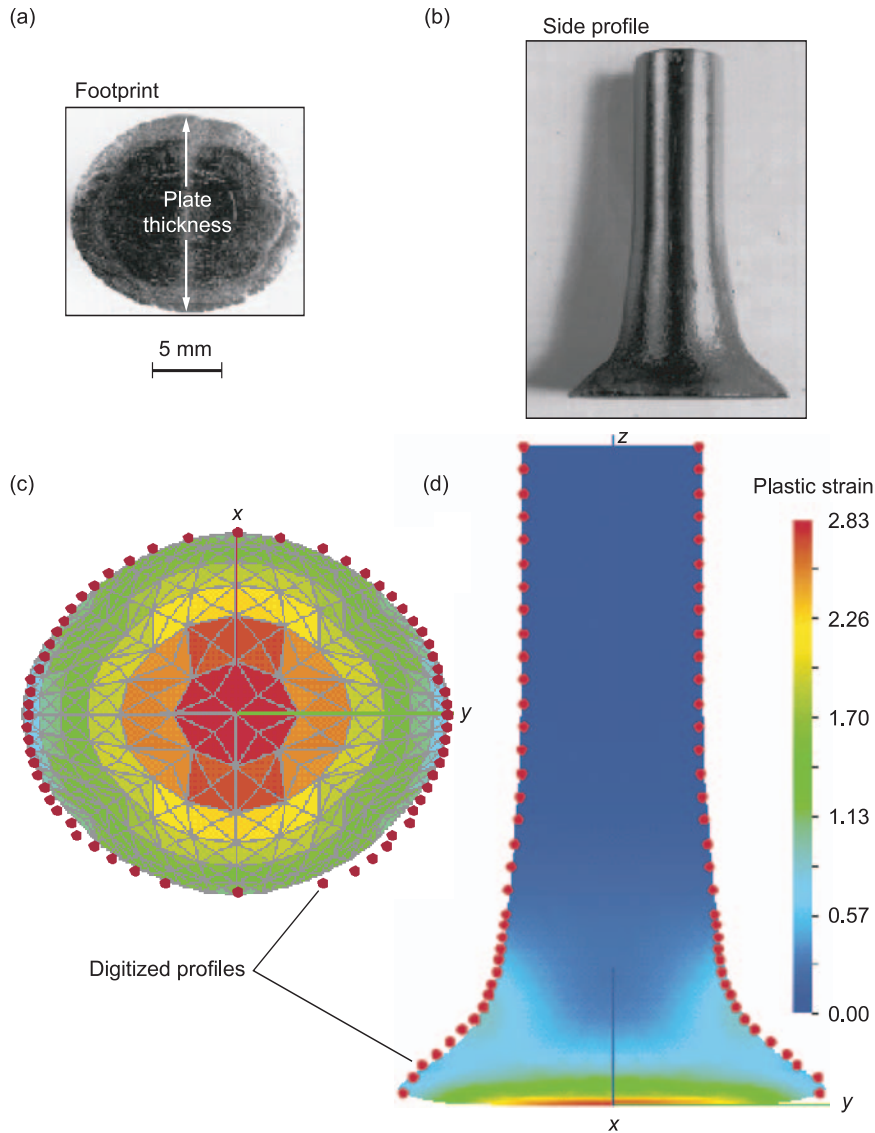


**Figure 5. Post-Test Geometry of Taylor Specimen and Simulation Results**

Photographs of the post-test geometry for a tantalum Taylor specimen show (a) the footprint and (b) the side profile. The colored patterns in (c) and (d) represent the plastic strain distribution predicted by the EPIC 3-D code simulation for the footprint and major side profile, respectively, of the Taylor sample. The red dots are the digitized experimental profiles.

presence of large gradients of stress, strain, and strain rate. Nevertheless, 3-D finite-element simulations of this integrated test have proved to be highly sensitive to the accuracy of material strength models used in the numerical codes. From a comparison of the cylinder profile of the post-test Taylor sam-

ple with the profile predicted by the finite-element code simulations, we have determined how well the material model and the code implementation describe the spatial gradients of deformation stress and the strain rates that ultimately lead to the final strain distribution seen at the end of the test.

The spatial stress and strain gradients and the strain rates, in turn, are direct measures of the stress-strain tensor described in the strength model. Moreover, based on tests conducted on copper, tantalum, aluminum, tungsten-nickel-iron alloy, and steels over a range of impact velocities, we have seen that the final strain distribution is sensitive not only to strain hardening, strain rate, and temperature, but also to crystallographic texture.

Figure 5 compares experimental and finite-element simulation results for a Taylor test specimen (Maudlin et al. 1999) of unalloyed tantalum that has a moderately strong crystallographic texture (that is, a directional dependency of its flow stress due to material processing). The cylinder had been initially cut from a rolled tantalum plate with a preferred texture (crystal orientations) associated with the rolling process. In this particular process, the  $\{111\}$  planes (that is, the major diagonal planes) of individual cubic crystals were most often stacked with the normals to the  $\{111\}$  planes aligned with the through-thickness direction of the plate, which represents a strong direction in this particular stock of tantalum. Because the Taylor cylinder was cut with its axis perpendicular to the through-thickness direction of the plate, the material strong direction is aligned perpendicular to the loading axis of the impact; thus, one transverse direction of the initially round Taylor rod is stronger than the other. Consequently, the impact and subsequent plastic deformation during the Taylor test produced an anisotropic mechanical response illustrated by the elliptical footprint and the side profile shown in Figures 5(a) and 5(b). After testing, we used an optical comparator to generate a digitized footprint of the cross-sectional area at the impact interface and digitized side profiles—see the red dots in Figures 5(c) and 5(d). We simulated the Taylor impact test with

the explicit, Lagrangian, finite-element code EPIC in a 3-D mode by using the MTS model for tantalum. The cylinder was spatially modeled using 4185 nodes and 17,280 single-integration-point tetrahedral elements. Because in the experiment both the anvil and cylinder base had mirror-like finishes and were carefully aligned for orthogonal impact, interfacial friction at impact at the cylinder-anvil interface was negligible and could be ignored in the simulation. Similarly, the vanishing hardness of the Taylor cylinder relative to that of the anvil precluded any measurable plastic compliance within the anvil, and so that too could be ignored. We simulated the impact event for 90 microseconds of problem time, after which plastic deformation reached quiescence, as it had in the experiment.

Calculational results of an impact-interface footprint and a late-time cylindrical major profile are shown in Figures 5(c) and 5(d). These results are compared with the experimental shapes indicated by red dots. The calculated elliptical footprint shown in Figure 5(c) has an eccentricity (ratio of major to minor diameters) of about 1.20 that compares well with the experimental footprints. If the sample were to have been isotropic, in which case the individual crystals would have been randomly oriented, it would have produced a round footprint with an eccentricity of 1. The major side profile compared with experimental data (red dots) in Figure 5(d) indicate that the final length agrees well with the experimental length and that the axial distribution of plastic strain also tracks very well with the experimental profile.

The MTS model was used together with an anisotropic yield surface whose tensor implementation of texture allows the modeling of crystalline texture. The combination pro-

duced very good agreement between the calculated and experimental plastic deformation field for the tantalum cylinder, including the anisotropic shape of the final cylinder. This example demonstrates the state of the art of 3-D mechanical modeling of yield anisotropy for a material subjected to a fairly complicated impact test, in which spatial variations in stress, strain, and strain rate occur simultaneously. Further work on materials demonstrating increasingly complicated deformation mechanisms as part of their mechanical stress-strain behavior will determine the direction of future mechanical-behavior model development.

### Validating Strain-Localization and Fracture Models

The Taylor test is a good example of bulk deformation in which spatial gradients of permanent plastic strain

extend over the entire sample—from 100 percent strain at the impact interface to near-zero strain at the opposite end of the cylinder. Under more extreme loading conditions, however, material instabilities can set in, causing plastic deformation to localize into planes that extend through the metal. Those localized regions of strain often appear as bands in the post-test specimen sections. Such material instability and plastic localization lead to the loss of load-carrying capacity and to damage evolution and fracture, as depicted on the right side (negative-slope region) of the stress-strain curve in Figure 1. In a typical tensile experiment, a material is pulled at constant strain rate, and its load-carrying capacity first increases (strain hardening). At some point, however, the load-carrying capacity reaches a maximum, and if the applied load remains constant or increases while the load-carrying capacity begins to decrease, a run-

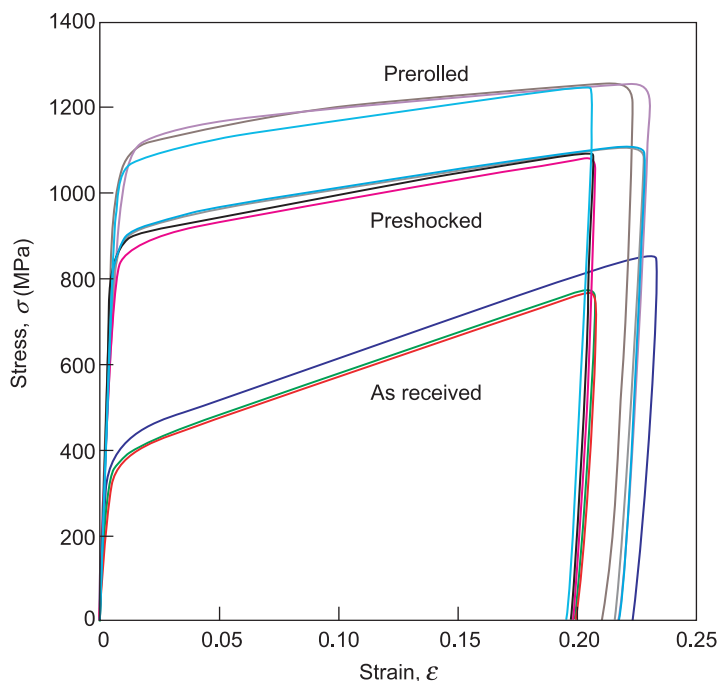


**Figure 6. Uniaxial Stress Compression Measurements**

The curves are of experimental stress vs strain for a stainless steel (SS316L) rolled-plate stock material. Shown are room temperature, quasistatic, and uniaxial-stress compression results as measured for the three SS316L conditions.



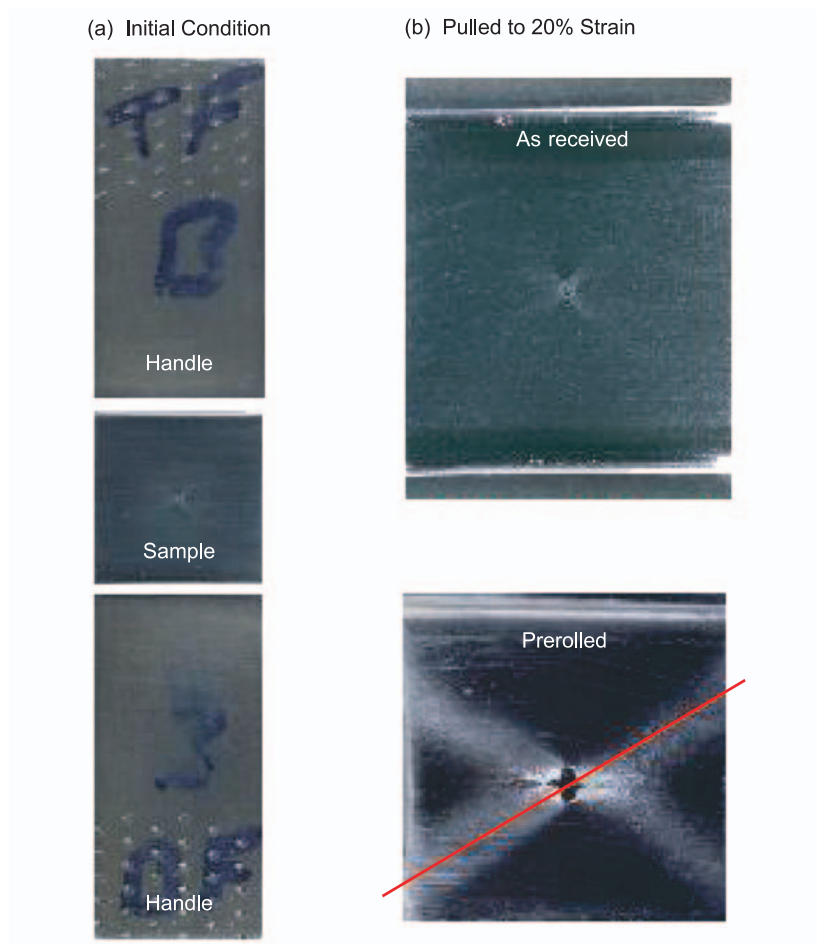


**Figure 7. Stainless Steel Flat-Plate Shear Specimens**

(a) The photograph is of a flat-plate SS316L sample of uniform-thickness rolled stock before the tensile test. The initial specimen geometry includes a small defect (hole) in the center of the sample. (b) The photographs are of two specimens after having been stretched quasistatically at room temperature to a 20% strain. The initial material states were as received (top) and prerolled (bottom).

away or unstable situation will occur with increasing strain. In many materials, this unstable motion results in localized deformation.

We have used a number of small-scale experiments, including pulling simple flat-plate samples, to study localized-strain and damage evolution as a function of the “starting state” of a material. The starting state could be a prerolled or preshocked process with an amount of flow stress hardening (slope of Figure 1)

that depends on the magnitude and direction of strain applied during preprocessing. In these experiments, small, uniaxial, square flat-plate tensile specimens (12.7 millimeters on one side and 1.0 millimeter in thickness) are cut from a stainless steel (SS316L) rolled-plate stock, either as received or preprocessed, and the specimens are then pulled to failure and insipient failure (about 40 percent longitudinal true strain).

Before the flat-plate testing, we

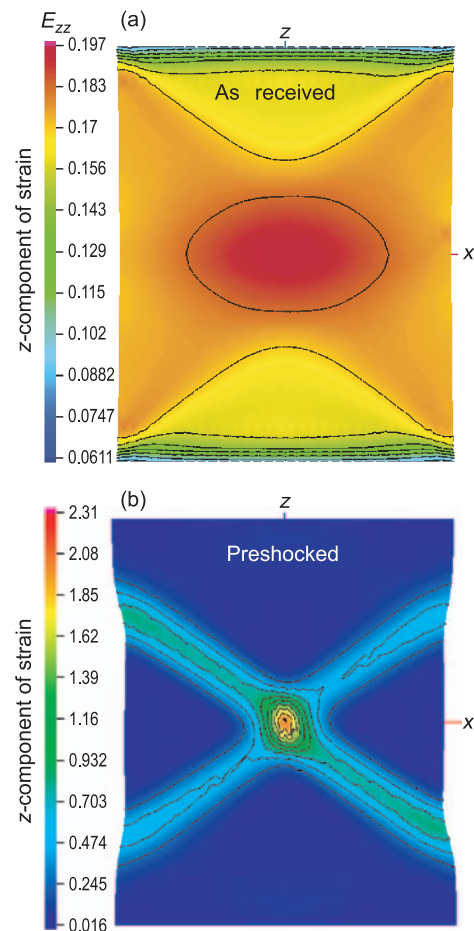


**Figure 8. Strain Distributions for Flat-Plate Shear Specimens**

Results of a 3-D finite-element simulation are shown in terms of the Lagrangian strain  $E_{zz}$  at 100  $\mu$ s into the deformation. Simulations use the MTS model for the stainless steel sample with an initial hole defect. Shown in (a) is the final strain state in the as-received material; in (b), deformation localizes into a shear band doublet in preshocked material.

measured the mechanical properties of the starting material by cutting cylindrical samples from the same preprocessed stock and subjecting them to uniaxial compression testing. Figure 6 compares flow stress curves from these tests for three material starting conditions: an as-received fairly ductile material, the same as-received material but prerolled by a 20 percent strain before testing, and the same as-received material but preshocked by a high-



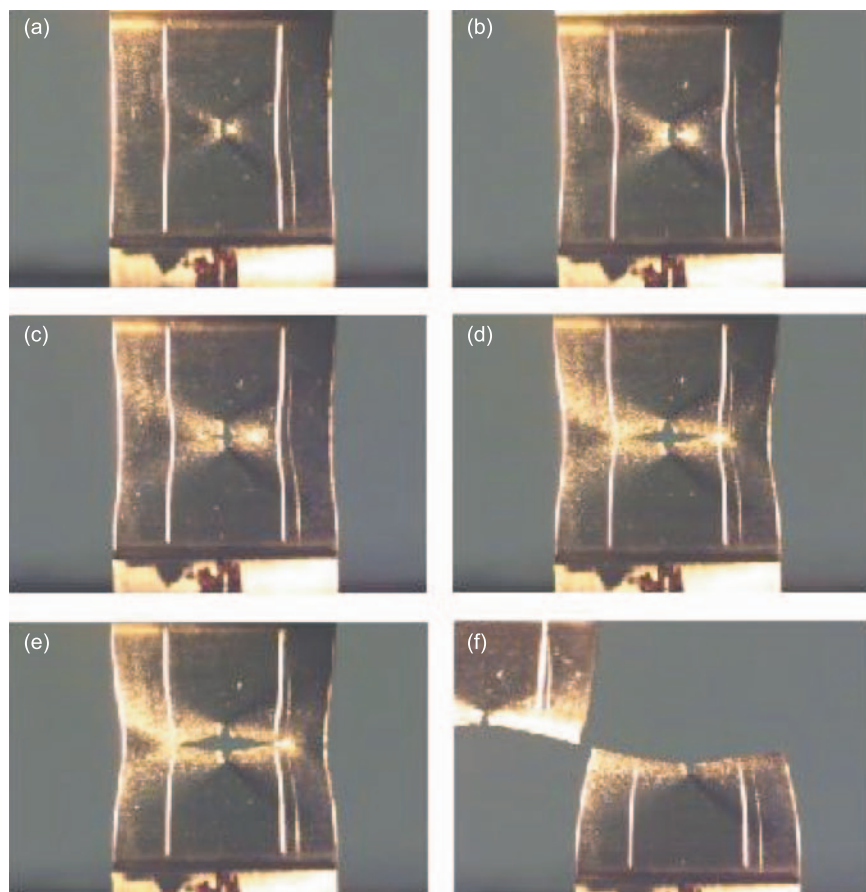


**Figure 9. SS316L Flat-Plate Shear Specimen—Late Deformation and Fracture Stages**

Dynamic photographs of an SS316L flat-plate shear specimen show it during the late stages of deformation and fracture. This test was conducted quasi-statically at room temperature for the initial, prerolled, hardened material condition. The initial specimen geometry has a small defect (hole) in the center of the gauge section. Time progresses from (a) to (f).

explosive (PBX-9501) plane detonation wave loading. The preshocked material has a higher flow stress and a lower slope than the as-received material. It is therefore less stable or closer to the point at which material instability initiates a transition from homogeneous to localized deformation. This reduction of stability in preshocked material is often relevant to defense applications. Figure 6 also shows that the prerolled material has even higher flow stress and lower slope, and therefore less stability, than the preshocked material.

The photographs in Figure 7(a)

show the geometry of the flat-plate tensile test, including the handles used to pull the sample. All the flat-plate test specimens have a small initial mechanical defect (hole) that has been machined into the center of the sample. Figure 7(b) shows magnified photographs of the as-received and the prerolled specimens after having been pulled to about 20 percent strain. These specimens exhibit post-yield (the strain exceeds the elastic limit) shear bands. In particular, each exhibits a strain localization doublet centered on the hole. The prerolled material is obviously much

more unstable. Compared with the as-received specimen, it exhibits a very prominent strain localization doublet. This higher susceptibility to instability and strain localization can be anticipated from the stress-strain results of Figure 6, in which the flow stress during plastic deformation is higher in magnitude and lower in slope for the prerolled specimen. The orientation of the localization doublet in the prerolled sample measured relative to a transverse specimen direction (a horizontal axis) is  $\beta \approx 30^\circ \pm 1^\circ$ .

In 1975, Rudnicki and Rice achieved a theoretical breakthrough by formulating a mathematical description of strain localization that treats the jump in material strain as a stationary wave discontinuity, formally analogous to the description of a shock wave as a traveling wave discontinuity. In many dynamic applications, localizations of strain lead to material damage (voids and cracks) and final failure of system components. The localization description developed by Rudnicki and Rice is a cornerstone in the material instability or bifurcation literature. The theory, which becomes applicable when the strength of a material becomes saturated (the stress reaches a maximum, and the slope of the stress-strain curve is zero or negative), predicts three items of interest: the onset of material instability, the orientation of the localization planes, and the direction of the straining jump in the localization band. Figure 8 shows our finite-element predictions for the SS316L as-received and preshocked samples. The simulations validate the fundamentals of the Rudnicki and Rice derivation, predict the background strain before the onset of localization, and predict the orientation of the localization planes. Deformation appears as mostly uniform, or homogeneous, in the as-received specimen—Figure 8(a)—in contrast with the preshocked speci-

men—Figure 8(b)—where it localizes into a doublet of shear bands. These simulations are then compared with experiments to validate the models. The predicted localization orientations are in good agreement with the test results. Despite the shear doublet apparent in the prerolled test specimen shown in Figure 7, all specimens in all three starting material conditions, with or without an initial defect, failed in a normal mode; that is, they fractured transversely across the specimen. The dynamic sequence of photos in Figure 9 shows the development of this horizontal fracture and reveals geometric specimen necking just before fracture. The latter implies a value of stress triaxiality (that is, ratio of pressure to flow stress) larger in magnitude than the uniaxial value of  $1/3$ . As confirmed by additional bifurcation analyses with the Rudnicki and Rice theory, this transition from uniaxial to higher-stress triaxiality, which causes more lateral restraint, is responsible for rotating the strain-localization planes and producing the appearance of a horizontal fracture; the photos show a fracture edge in the observation plane, where a macro crack runs in the horizontal direction across the section intersecting the hole. This localization and fracture phenomenology manifests itself in the context of explosive loading problems involving more complex states of stress, as will be discussed in the next section.

### Validating Models for Explosively Driven Dynamic Deformation

Many defense applications at Los Alamos involve explosively driven systems in which the materials are subjected to extreme conditions of temperature and strain rate. Our ultimate goal for modeling and simulation is to develop the ability to predict

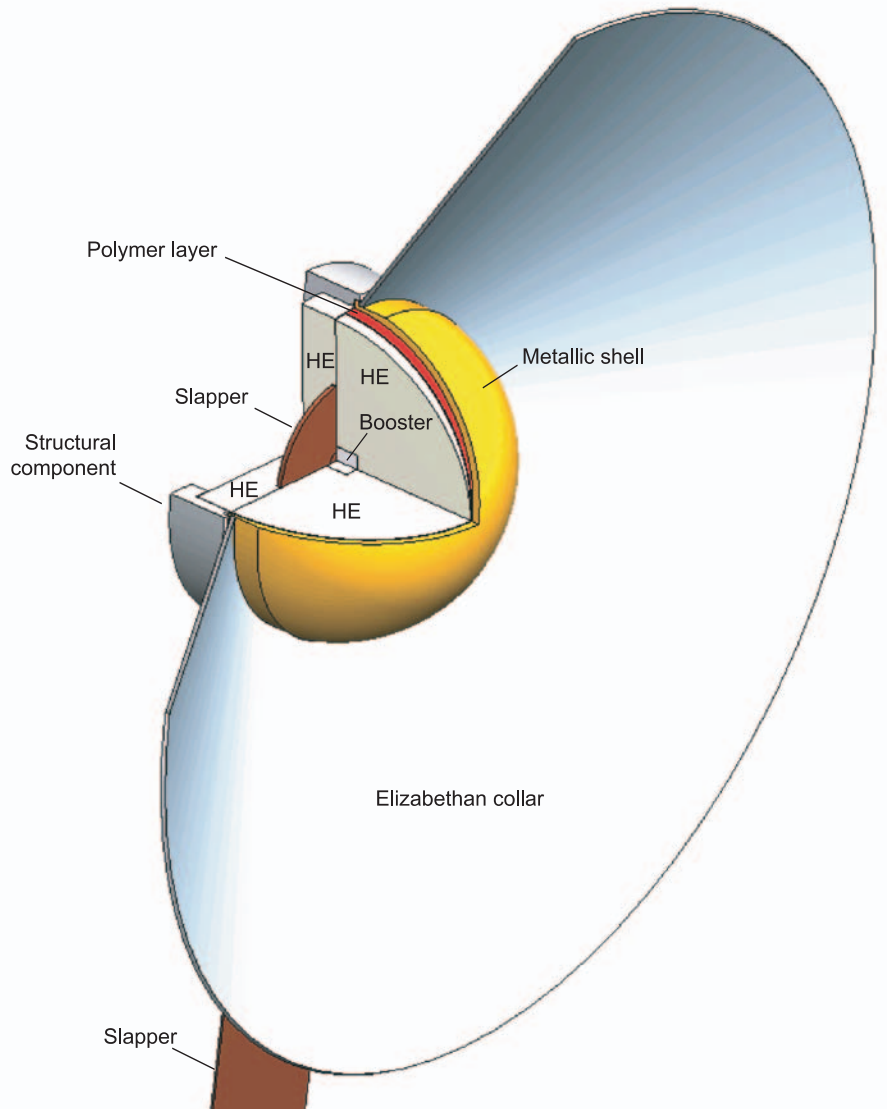


**Figure 10. Solid Model of the Filled-Hemishell Experimental Hardware**  
The experiment conducted with this hardware was designed to reproduce as closely as possible a spherical detonation inside a metal hemishell.

the onset of strain localization in shells of arbitrary geometry, the coalescence of those localizations into a network of cracks as a precursor of fracture, the fracture of the shell into individual fragments, and the size, velocity, and spatial distribution of those fragments. We must be able to model and simulate the correct physics for a broad variety of materials that are manufactured into a shell geometry and tested under various loading configurations. In this section,

we describe small-scale integrated tests involving high explosives that are exploited as another source of validation data (albeit, more complicated and challenging than, for example, the flat-plate tensile specimens above) for modeling and simulation. One such test is the explosively driven hemispherical shell. In the simulation of this experiment, a hemispherical metal shell filled with explosive is initiated at the spherical center. Radial propagation of the spherical detonation

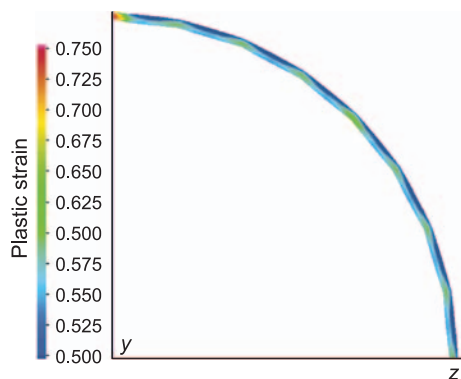


**Figure 11. Predicted Strain Distribution of the Filled Hemishell**

This calculation used as-received material strength properties. The plastic strain is the plotted field variable. The results show fairly uniform deformation.

wave results in the simultaneous arrival of the wave at the explosive-metal interface.

**Experimental Design.** A hemisphere is filled with high explosive (PBX-9501) whose density is 1.833 grams per cubic centimeter ( $\text{g/cm}^3$ ). Both the explosive and metal are highly characterized in terms of mechanical properties and process control. Also, no effort was spared to make the fielded design as close to the idealized geometric configuration as possible and to facilitate a clear view of the fracture process (see Figure 10). For example, the high-explosive slapper system for initiating the detonation was designed to approximate as closely as possible the mathematical idealization of a detonation initiated at a single point. The booster pellet is embedded in the main charge so that the initiation system should not perturb the explosive drive at the pole. There is also no metal case around the booster, and the slapper itself is a thin copper/plastic laminate system that generates a minimal amount of debris that could contaminate the optical view of the fracture process. The fixture that holds the

hemishell configuration in space is a thin (0.75-millimeter) “Elizabethan collar” made from spun aluminum. The collar provides a lightweight but robust symmetrical mount for the shot. A 5-millimeter-thick disk of explosive holds the initiation assembly in place, and a polycarbonate ring holds the explosive, collar, and metal shell in place. As the shell expands, the explosive interacts with the collar and pushes it out of the region of interest. The collar also disperses the debris from the slapper initiator and increases the late push on the hemishell’s equator. These design elements cause the motion of the shell to approximate more closely a spherical expansion.

The filled-hemishell design is more attractive for modeling and simulation validation activities than the classic design of end-detonated filled-cylinder devices. The filled hemishell prevents the seeding of strain localizations that occur in filled cylinders when the detonation wave sweeps from one end to the other along the explosive/metal interface. The spherical symmetry of the detonation in the filled hemishell thus allows direct observation of strain localization, controlled by the material instability and bifurcation concepts discussed above. The resulting nearly spherical expansion of the shell causes predominantly biaxial stress, resulting in fragments with aspect ratios near unity, and maintains axis symmetry so that the 3-D effects observed in the shell fragmentation process can be linked to the fracture process itself. Finally, because the test configuration is small, various diagnostics, including proton radiography, become quite feasible for this integrated test.

**Simulation Results for a U6Nb Hemishell.** Three-dimensional finite-element simulations of the filled hemispherical shell of uranium alloyed with 6 percent niobium were conduct-

ed with the material modeling described above. U6Nb is a good test of our modeling capability because tensile tests, such as the flat-plate tensile tests described above, have shown preshocked U6Nb to be more unstable with a strong propensity to strain-localize when compared with most metals. Figure 11 shows predictions of the plastic strain distribution in a centerline section of the U6Nb shell for a stable, as-received material condition, showing fairly uniform deformation (plastic strain ranging from 0.5 to 0.75); these results correspond to a time of 5 microseconds after the detonation wave loads the shell. The computations were performed with the EPIC finite-element code with the goal of predicting the onset of material instability in the U6Nb material. The 3-D shell shown in Figure 12 shows pronounced strain localization (the plastic strain reaches 1.0 in several cells, whereas most of the hemishell has a strain of about 0.6), resulting from the unstable material character of shock-processed U6Nb. The shell expands axisymmetrically at small times, while the material is still stable, but quickly loses this symmetry and exhibits 3-D effects as strain localizations develop.

The simulation results are consistent with our understanding of material instability and strain localization; the critical strain at which the material loses stability increases as the hardening modulus (the slope on the stress-strain curve of Figure 1) increases, and it decreases as the magnitude of the flow stress increases. The main effects of preshock on U6Nb are to raise the initial flow stress and to significantly reduce the hardening modulus. Consequently, the shock-hardened U6Nb becomes unstable shortly after the detonation wave loads the shell, and subsequently the strain localizes, and the shell expands nonuniformly.



### Experimental vs Simulation

**Results.** The EPIC predictions were compared with the experimental results from the corresponding filled-hemishell test. Both proton radiographs taken during shell expansion and the fragments recovered following the shots yield experimental information on the onset of strain localization. Figure 13 presents proton radiographs viewed normal to the pole of the hemishell at different times. Localized thinning is apparent at an early time (8.2 microseconds)—Figure 13(b). At a later time, these localizations coalesce into an ultimate fragmentation pattern—Figure 13(c). Supporting fragment recovery experiments that use a water medium have yielded significant information on the failure of the filled hemishell. In these recovery experiments, the shell is initially immersed into water so that there is no metal/water impact that could induce additional material damage. The recovered fragments represent an approximation to the conditions at the time at which fragmentation is complete (the fragments are fully separated from each other, as shown in the 16.8-microsecond radiograph of Figure 13).

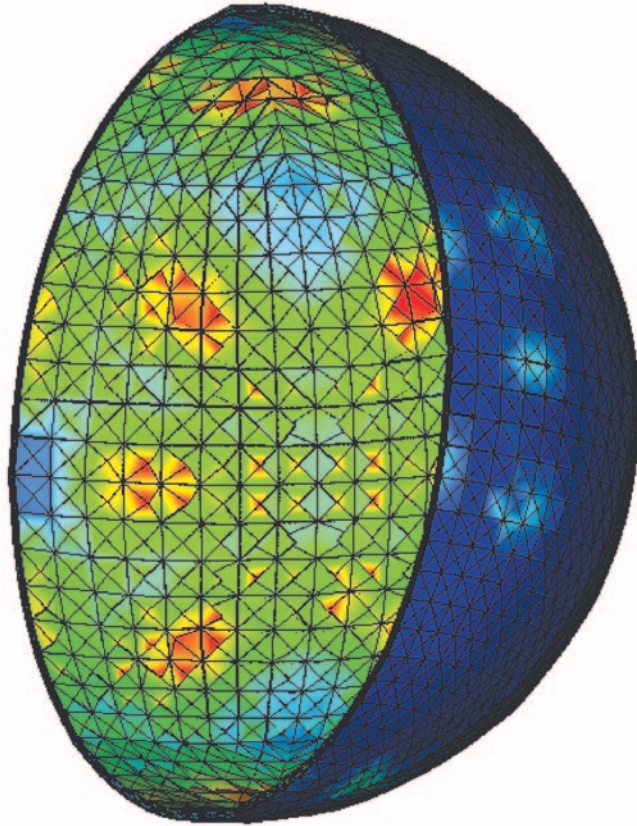
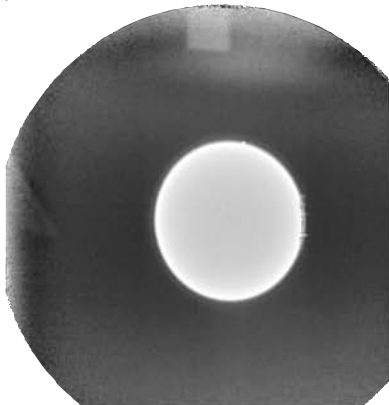


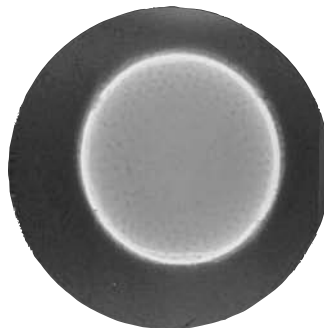
**Figure 12. Predicted Strain Distribution of the Preshocked Filled Hemishell**

For this calculation, we used shocked material strength properties. Plastic strain is the field variable indicated as color contours. Development of pronounced strain localization is apparent.

(a)  $t = 0$



(b)  $t = 8.2 \mu\text{s}$



(c)  $t = 16.8 \mu\text{s}$

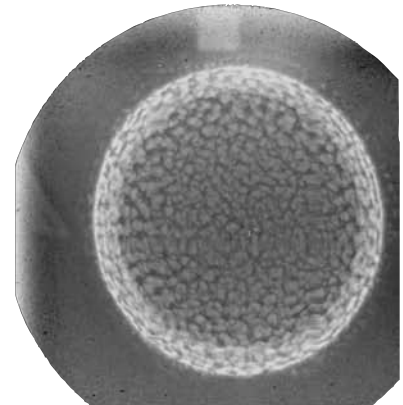


**Figure 13. Unstable Expansion of a Filled Hemishell Shown by Proton Radiographs**

The proton radiographs taken during shell expansion yield experimental information on the onset of strain localization. Localized thinning is apparent, which then develops into a fragmentation pattern at 16.8  $\mu\text{s}$ .

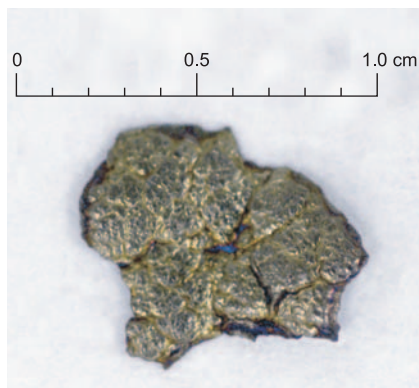


**Figure 14. Photograph of a U6Nb Fragment**

This photograph of a fragment recovered with a water medium reveals a free surface with many strain-localized features.

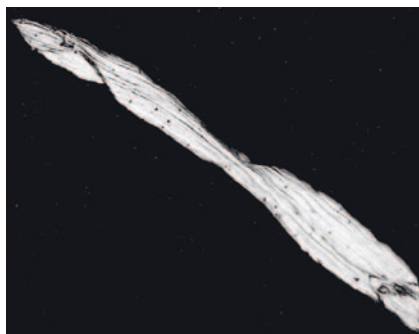


**Figure 15. Edge Micrograph of a U6Nb Fragment**

This is a microscopic side view of the fragment shown in Figure 14.

A surface photograph of a recovered fragment (Figure 14) reveals a free surface sculptured by many strain-localized features. Evidently, some strain localizations dominate and coalesce to form the fragments, while the growth of others is arrested as a natural consequence of the competition among localizations to accommodate the loading and boundary conditions. Figure 15 shows a microscopic side view of the fragment, obtained by a cut on a plane normal to the free surface. In regions distant from localizations, the background strains are relatively large at about 60 percent. Interestingly, the defects

(for example, grain boundaries, niobium concentration bands, and carbide inclusions) that one might expect to influence the strain localization distribution appear not to be responsible for the initiation, or nucleation, of the localization phenomenology.

The experimental data support the computations qualitatively and, to some degree, quantitatively. At 8 microseconds, strain localization is evident in the experiment as thinning occurs in small areas. The recovered fragments show background strains of about 60 percent, and this value compares well with the predicted background strain at 8 microseconds, provided we assume that, when localization begins, the background strain ceases to increase and all the subsequent strain is concentrated in the localizations. The validity of this assumption remains to be checked. Also, since the physical basis for the nucleation of strain localization has not been identified in the simulations, we only expect the predicted distribution to roughly match the experimentally determined spatial distribution of thinned areas.

In summary, the shell experiments have validated our modeling and simulation capability to predict when a metal will bifurcate into localized strain, provided we have an accurate mechanical representation at the relevant conditions.

## Conclusions

The Taylor cylinder impact test, the plane-strain tensile test, and explosively driven hemisphere test represent readily conducted experiments that probe the deformation, damage evolution, and fracture behavior of materials. Because these tests are very sensitive to large gradients of stress, strain, strain rate, and shock loading, we are using them to evaluate and validate the correctness of our mechanical models

that are implemented and destined to be implemented into large-scale 3-D simulation codes.

Robust models that capture the physics of high-rate material response are required for developing predictive capability for highly dynamic events. The increased effort to link experiments and modeling within the computational mechanics community and the increased emphasis on code verification and validation within the Los Alamos National Laboratory defense programs are accelerating this development. These efforts are already receiving recognition through the recent establishment of verification and validation committees within various technical societies. ■

## Further Reading

- Chen, S. R., and G. T. Gray III. 1996. Constitutive Behavior of Tantalum and Tantalum-Tungsten Alloys. *Metall. Mater. Trans. A* **27** (10): 2994.
- Gray III, G. T. 2000. Classic Split-Hopkinson Pressure Bar Technique. In *ASM-Handbook*, Vol. 8, Mechanical Testing and Evaluation, p. 462. Edited by H. Kuhn and D. Medlin. Metals Park, Ohio: ASM International.
- Maudlin, P. J., J. F. Bingert, J. W. House, and S. R. Chen. 1999. On the Modeling of the Taylor Cylinder Impact Test for Orthotropic Textured Materials: Experiments and Simulations. *Int. J. Plasticity* **15**: 139.
- Rudnicki, J. W., and J. R. Rice. 1975. Conditions for the Localization of Deformation in Pressure-Sensitive Dilatant Materials. *J. Mech. Phys. Solids* **23**: 371.
- Taylor, G. I. 1948. The Use of Flat-Ended Projectiles for Determining Dynamic Yield Stress. I. Theoretical Considerations. *Proc. R. Soc. London, Ser. A* **194** (1038): 289.

*For further information,  
contact George T. Gray III (505) 667 5452  
(rusty@lanl.gov).*